

# On the self-consistent time-dependent linearized response of stellar discs to external perturbations

D. Dootson,<sup>1</sup> J. Magorrian<sup>1</sup>★

<sup>1</sup>*Rudolf Peierls Centre for Theoretical Physics, Clarendon Laboratory, Parks Road, Oxford OX1 3PU*

Accepted XXX. Received YYY; in original form ZZZ

## ABSTRACT

We study the explicitly time-dependent response of a razor-thin axisymmetric disc to externally imposed perturbations by recasting the linearized collisionless Boltzmann equation as an integral equation and applying Kalnajs’ matrix method. As an application we consider the idealized problem of calculating the dynamical friction torque on a steadily rotating, two-dimensional bar. We consider two choices of basis functions in the matrix method, showing that both lead to comparable results. The torques from our linearised calculation are in excellent agreement with those measured from  $N$ -body simulation, as long as the bar perturbation does not resonate with a significant fraction of the disc’s stars.

**Key words:** galaxies: kinematics and dynamics – methods: analytical

## 1 INTRODUCTION

$N$ -body simulation is the single most powerful technique for probing collisionless stellar dynamics. Although  $N$ -body simulations are superficially easy to run, setting them up and interpreting their results is often difficult: they rely on Monte Carlo sampling the galaxy’s phase space distribution function (hereafter DF) (e.g., [Leeuw et al. 1993](#)), which can require prohibitively large  $N$  to ensure that both the DF and the gravitational potential it sources are sufficiently well sampled. Nevertheless, much of our understanding of stellar dynamics comes from carefully controlled  $N$ -body simulations (e.g., [Sellwood 2012](#)).

An alternative to  $N$ -body simulation is to use finite element methods to solve the collisionless Boltzmann equation (CBE) for the evolution of the DF directly (e.g. [Mangeney et al. 2002](#); [Colombi et al. 2015](#)). These allow the development of fine structure in the DF to be followed in exquisite detail, but for now are prohibitively expensive to apply to any but the most favourable problems.

There are many problems for which these very general numerical methods are overkill. For example, many physical processes (e.g., dynamical friction, spiral arm formation) are most naturally thought of as taking place against the backdrop of some underlying equilibrium state. If we can assume that the galaxy is close to equilibrium and that any perturbation

forces only a small departure from this initial state, then it is sensible to focus first on the linearised response of the galaxy to the perturbation. The resulting linearised evolution equations are easy to solve (albeit sometimes only formally) and are a first step into gaining insight into the full nonlinear evolution.

Techniques for computing the direct solution of the linearised CBE have been less widely applied than their  $N$ -body counterparts. The simple reason for this is that stars do not move in straight lines, but instead have complex orbits in real-space coordinates  $(\mathbf{x}, \mathbf{v})$ . Instead of working with these  $(\mathbf{x}, \mathbf{v})$  orbits directly – as one would in an  $N$ -body simulation – one has to transform the CBE into action-angle coordinates,  $(\boldsymbol{\theta}, \mathbf{J})$  ([Arnold 1987](#)), a coordinate system in which stars move in straight lines, making it possible to write down the solution to the CBE.

However, this results in a problem: the CBE is closed under Poisson’s equation – as the stars’ potential ultimately governs their evolution – which is most naturally solved in real space coordinates (i.e.,  $\mathbf{x}$ ). The mathematical complexities of this paper are ultimately concerned with this tension between the  $(\boldsymbol{\theta}, \mathbf{J})$  coordinates used to solve the CBE and  $(\mathbf{x}, \mathbf{v})$  for Poisson’s equation. We address it using the approach first laid out in [Kalnajs \(1971\)](#), by projecting solutions of the CBE onto a basis – the so called potential-density pairs – that by construction solve Poisson’s equation.

One way of solving the resulting linearised CBE–Poisson equations is by Fourier transforming in time (e.g. [Pichon &](#)

★ E-mail: john.magorrian@physics.ox.ac.uk

Cannon 1997; Evans & Read 1998; De Rijcke et al. 2019), which leads to a pleasingly simple algebraic equation for the frequency dependence of the response. This is appropriate if one wants to test the stability of an isolated galaxy or to compute its response to an eternal, perfectly periodic perturbation. For more general scenarios, however, this transformation from time to frequency is an unnecessary obfuscation and it makes more sense to solve for the time evolution directly.

Although much work has been done to study the response of a self-gravitating system to an external perturbation, most have overcome the complications highlighted in the previous paragraphs by making one of three assumptions: simplification of the geometry or relying on the epicycle approximation to result in simple equations of motion (e.g., Julian & Toomre 1966; Fouvry et al. 2015; Magorrian 2021); ignoring the contribution to the potential from the self-consistent response (i.e., removing the need to close the CBE under Poisson’s equation) (e.g., Colpi & Pallavicini 1998; Monari et al. 2016); prescribing the time dependence of the external perturbation without allowing it to change according to the galaxy’s response (e.g. Banik & van den Bosch 2021; Al Kazwini et al. 2022).

To date only Murali (1999) and Rozier et al. (2022) have solved the general self-consistent time evolution of the linearised CBE in action-angle variables using potential-density pairs. The present paper follows in the vein of these works, but instead of studying the response of a halo we tackle the more modest problem of computing the response of a 2D razor-thin disc to a external perturbation.

In section 2 we establish our notation and review the derivation of the integral equation that governs the evolution of the disc’s density response. In Section 3 we show how to calculate the explicitly time-dependent response of a razor-thin disc model, comparing the performance of two distinct choices of potential–density pairs (Kalnajs 1976). Section 4 presents a calculation of the Green’s function of the system, the object at the heart of all initial value analyses. As a straightforward application in Section 5 we calculate the dynamical friction torque exerted by the disc on an externally imposed bar and compare the results to those measured in  $N$ -body simulations. We first do this for a weak bar, confirming the predictions of linear theory, before showing the discrepancy due to non-linear phenomena when a stronger bar is used. Appendix A explains how we calculate our evolution kernel. For completeness, Appendix B gives details of the Kalnajs basis functions we use and Appendix C summarises the details of our  $N$ -body simulations.

## 2 DYNAMICAL EVOLUTION

Consider a galaxy that is in equilibrium with its stars orbiting in a steady potential  $\Phi(\mathbf{x})$  and having phase space mass density function  $F(\mathbf{x}, \mathbf{v})$ . This equilibrium is perturbed by an externally imposed potential,  $\epsilon\psi^e(\mathbf{x}, t)$ . In response, the

stars’ DF changes from  $F(\mathbf{x}, \mathbf{v})$  to  $F(\mathbf{x}, \mathbf{v}) + \epsilon f(\mathbf{x}, \mathbf{v}, t)$ , with the change  $\epsilon f$  in the DF adding  $\epsilon\psi^f(\mathbf{x}, t)$  to the gravitational potential of the system. The subsequent evolution of the galaxy is governed by the CBE,

$$\frac{\partial}{\partial t}(F + \epsilon f) + [F + \epsilon f, H] = 0, \quad (1)$$

with Hamiltonian  $H = H_0 + \epsilon\psi$ , in which we assume that  $H_0 \equiv \frac{1}{2}\mathbf{v}^2 + \Phi$  and the perturbation potential

$$\psi = \psi^e + \psi^f, \quad (2)$$

is the sum of the externally imposed stimulus  $\psi^e$  plus the galaxy’s response  $\psi^f$ . The latter is related to the DF response  $f$  through Poisson’s equation,

$$\nabla^2\psi^f = 4\pi G \int d\mathbf{v} f. \quad (3)$$

We assume that angle-action variables  $(\boldsymbol{\theta}, \mathbf{J})$  exist for the unperturbed galaxy’s Hamiltonian  $H_0$ . It is natural then to express the response DF  $f$  as a Fourier series in the angles,

$$f(\boldsymbol{\theta}, \mathbf{J}) = \sum_{\mathbf{m}} f_{\mathbf{m}}(\mathbf{J}) e^{i\mathbf{m} \cdot \boldsymbol{\theta}}, \quad (4)$$

with analogous expansions for  $\psi^e$  and  $\psi^f$ . Invoking Jeans’ theorem we may assume that  $F = F(\mathbf{J})$  only (Binney & Tremaine 2008). Substituting these expansions into (1) and dropping the  $O(\epsilon^2)$  terms, the linearised evolution equation for the response DF is

$$\frac{\partial f_{\mathbf{m}}(\mathbf{J}, t)}{\partial t} + i\mathbf{m} \cdot \left[ \boldsymbol{\Omega}(\mathbf{J}) f_{\mathbf{m}}(\mathbf{J}, t) - \frac{\partial F(\mathbf{J})}{\partial \mathbf{J}} \psi_{\mathbf{m}}(\mathbf{J}, t) \right] = 0, \quad (5)$$

where we have defined  $\boldsymbol{\Omega}(\mathbf{J}) \equiv \partial H_0 / \partial \mathbf{J}$ .

One way to proceed from here would be to Fourier transform in time in order to remove the derivative in the first term, resulting in a simple algebraic equation for the (transformed) response. As noted in the introduction, this is the route adopted by most previous work on the linearised CBE. Instead we follow the approach taken in Murali (1999) and note that the formal solution to (5) assuming that the galaxy started in equilibrium in the distant past is simply

$$f_{\mathbf{m}}(\mathbf{J}, t) = i\mathbf{m} \cdot \frac{\partial F}{\partial \mathbf{J}} \int_{-\infty}^t dt' e^{-i\mathbf{m} \cdot \boldsymbol{\Omega}(\mathbf{J})(t-t')} \psi_{\mathbf{m}}(\mathbf{J}, t'). \quad (6)$$

The complication is that the  $\psi_{\mathbf{m}} = \psi_{\mathbf{m}}^e + \psi_{\mathbf{m}}^f$  factor in the integrand depends on  $f_{\mathbf{m}}$  through Poisson’s equation (3). Following Kalnajs (1976), we deal with this by introducing a complete set of potential–density pairs  $(\psi^\mu(\mathbf{x}), \rho^\mu(\mathbf{x}))$ , the elements of each pair  $\mu$  being related by Poisson’s equation

$$\nabla^2\psi^\mu = 4\pi G \rho^\mu. \quad (7)$$

For any choice of basis there is a matrix

$$\mathcal{E}^{\mu\nu} = - \int d\mathbf{x} \psi^\mu(\mathbf{x}) \star \rho^\nu(\mathbf{x}), \quad (8)$$

that describes how the elements of basis pairs  $\mu$  and  $\nu$  are

related. We expand the external potential and the induced response<sup>1</sup>

$$\psi^e(\mathbf{x}, t) = A_\mu(t)\psi^\mu(\mathbf{x}), \quad (9a)$$

$$\psi^f(\mathbf{x}, t) = B_\mu(t)\psi^\mu(\mathbf{x}), \quad (9b)$$

with expansion coefficients  $A_\mu(t)$  and  $B_\mu(t)$  respectively. In principle the number of terms in this sum is infinite, but in practice these expansions will be limited to a finite number of terms.

We are now in a position to combine Equation 6, which gives the evolution of the DF in the action-angle coordinate system, with our potential density pairs, that will allow us to easily incorporate self-gravity despite working in action-angle coordinates. Multiplying (8) by  $B_\nu$  and substituting  $\rho^f = B_\nu \rho^\nu = \int f d\mathbf{v}$  gives

$$\mathcal{E}^{\mu\nu} B_\nu = - \int d\mathbf{x} d\mathbf{v} f(\mathbf{x}, \mathbf{v}, t) \psi^\mu(\mathbf{x}). \quad (10)$$

As  $(\mathbf{x}, \mathbf{v})$  and  $(\boldsymbol{\theta}, \mathbf{J})$  coordinate systems are canonical, we can replace the integral over  $d\mathbf{x} d\mathbf{v}$  here by one over  $d\boldsymbol{\theta} d\mathbf{J}$ . Then taking  $f$  from equation (6) we have that

$$\mathcal{E}^{\mu\nu} B_\nu(t) = \int_{-\infty}^t dt' \mathcal{K}^{\mu\nu}(t-t') [A_\nu(t') + B_\nu(t')], \quad (11)$$

which is a linear Volterra equation for the evolution of our system. The kernel,  $\mathcal{K}^{\mu\nu}$ , is given by

$$\mathcal{K}^{\mu\nu}(t-t') = -i(2\pi)^d \times \int d\mathbf{J} \sum_{\mathbf{m}} \mathbf{m} \cdot \frac{\partial F(\mathbf{J})}{\partial \mathbf{J}} e^{-i\mathbf{m} \cdot \boldsymbol{\Omega}(\mathbf{J})(t-t')} \psi_{\mathbf{m}}^\mu(\mathbf{J})^* \psi_{\mathbf{m}}^\nu(\mathbf{J}), \quad (12)$$

where  $d$  is the dimensionality of configuration space. The same pair of equations (11) and (12) are derived in Murali (1999) and Rozier et al. (2022).

Given an external perturbation  $A_\nu(t)$  it is straightforward to solve Equation (11) numerically for the unknown response coefficients  $B_\nu(t)$  once the kernel (12) and the orthogonality matrix (8),  $\mathcal{E}$ , have been constructed. Moreover, because the numerical solution for the response  $B_\nu(t)$  at time  $t$  depends only on  $A_\nu(t')$  at times  $t' \leq t$ , we are offered the possibility of modifying the external perturbation  $A_\nu(t + \Delta t)$  at the next timestep to account for the effect of the response  $B_\nu(t)$ : such an opportunity is not afforded by methods that work in the frequency domain.

By introducing potential-density pairs (following Kalnajs 1976) we have reduced our problem to one of matrix arithmetic. There is however, no free lunch. By expanding in potential-density pairs, we have embedded Poisson's equation into our formalism. Although this has allowed us to

<sup>1</sup> For brevity we adopt the convention that repeated basis-function indices, such as  $\mu$  here, are summed over. To highlight the difference with Fourier indices  $\mathbf{m}$  (e.g. equation 4), for which the sum will always be explicit, we use the convention that indices belonging to basis functions are Greek.

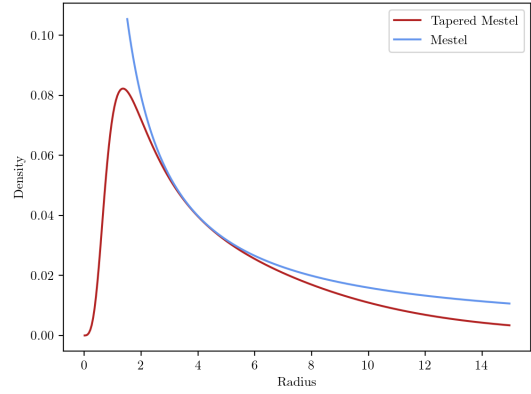


**Figure 1.** The density distribution for the tapered and untapered Mestel discs. The inner taper is at  $R = 1$  and the outer is at  $R = 10$ .

trivially include self-gravity, it has come at the cost: from Equation 11 we can only solve for the real space response rather than the full phase space response. In principle, however, this problem can be rectified as once the potential evolution is determined, Equation 6 can be solved to obtain the full phase space evolution.

The kernel given in Equation 12 has an intimate relationship to the response matrix,  $\hat{\mathcal{M}}^{\mu\nu}(\omega)$  (e.g. Binney & Tremaine 2008), as it represents how a disk will respond to an external perturbation and its own response. In fact, an expression for the response matrix can be obtained by applying the temporal Fourier transform  $\hat{A}_\nu(\omega) \equiv \int_{-\infty}^{\infty} A_\nu(t) e^{i\omega t} dt$  (and similarly for  $B_\nu$ ) to Equation 11. The result is

$$\mathcal{E}^{\mu\nu} \hat{B}_\nu(\omega) = \hat{\mathcal{M}}^{\mu\nu}(\omega) [\hat{A}_\nu(\omega) + \hat{B}_\nu(\omega)], \quad (13)$$

where the response matrix

$$\hat{\mathcal{M}}^{\mu\nu}(\omega) = -i(2\pi)^d \int d\mathbf{J} \sum_{\mathbf{m}} \mathbf{m} \cdot \frac{\partial F(\mathbf{J})}{\partial \mathbf{J}} \frac{\psi_{\mathbf{m}}^\mu(\mathbf{J})^* \psi_{\mathbf{m}}^\nu(\mathbf{J})}{\omega - \mathbf{m} \cdot \boldsymbol{\Omega}(\mathbf{J})}, \quad (14)$$

is the Fourier transformed kernel (12). Although this reduces the integral equation (11) to a simple matrix equation, it introduces an  $\omega - \mathbf{n} \cdot \mathbf{J}$  denominator that will inevitably vanish, causing much of the difficulties in the frequency-based analysis.

### 3 APPLICATION TO RAZOR-THIN AXISYMMETRIC DISCS

In this paper we use a razor-thin Mestel (Mestel 1963) disc as our underlying equilibrium model and will focus on its response to in-plane perturbations. There are more realistic disc models, but the simple DF and scale-free potential make

the Mestel disc popular for linear response work. In equilibrium the disc's potential is  $\Phi(R) = v_c^2 \log(R/R_0)$  where  $v_c$  is the circular orbit speed that sets the mass scale of the disk. The integrals of motion are the specific energy  $E$  and angular momentum  $L$ , in terms of which the disc's DF is given by

$$F_{\text{Mestel}}(E, L) = N L^q e^{-E/\sigma_R^2}, \quad (15)$$

where the free parameter  $\sigma_R^2$  sets the disc's temperature and the auxilliary variable  $q \equiv v_c^2/\sigma_R^2 - 1$ . The normalisation factor,

$$N = \frac{v_c^2}{2^{1+q/2} \pi^{3/2} G \sigma_R^2 \Gamma(1/2 + q/2)}, \quad (16)$$

is chosen so that the mass density  $\rho_{\text{Mestel}}(R) = \int d^2\mathbf{v} F_{\text{Mestel}} = v_c^2/(2\pi G R)$ , consistent with Poisson's equation.

In order to deal with the singularity at the centre of the disk and the infinite extent of the Mestel disk we follow the approach taken in [Sellwood & Carlberg \(2014\)](#) and [Fouvry et al. \(2015\)](#) and introduce inner and outer tapers to the DF,

$$T_{\text{inner}}(L) = \frac{L^{\nu_t}}{(R_i v_c)^{\nu_t} + L^{\nu_t}}, \quad (17)$$

$$T_{\text{outer}}(L) = \left[ 1 + \left( \frac{L}{R_o v_c} \right)^{\mu_t} \right]^{-1}. \quad (18)$$

The parameters  $\nu_t$  and  $\mu_t$  set the sharpness of the inner and outer taper respectively with  $R_i$  and  $R_o$  setting their location. We also assume that only a fraction  $0 < \xi \leq 1$  of the disk is active. Therefore, the DF of “live” stars that are free to respond to perturbations is given by

$$F(E, L) = \xi T_{\text{inner}}(L) T_{\text{outer}}(L) F_{\text{Mestel}}(E, L). \quad (19)$$

To set the overall scale of our disc we take  $v_c = G = R_0 = 1$ . For the distribution function we adopt the same parameters as [Sellwood & Carlberg \(2014\)](#) and [Fouvry et al. \(2015\)](#), namely  $\nu_t = 4$ ,  $\mu_t = 5$ ,  $R_i = 1$ ,  $R_o = 10$  and  $\xi = 1/2$ . We take  $\sigma_r = 0.35$ , unless otherwise specified.

Where appropriate we express times in terms of the dynamical time at the location of the inner taper – the time taken to complete a circular orbit there. This is  $T_{\text{dyn}} = 2\pi R_i/v_c = 2\pi$ .

### 3.1 Potential basis functions

We take advantage of the axisymmetry of the background DF and decompose our basis functions as

$$\psi^\mu(r, \phi) = e^{i\ell\phi} \mathcal{U}_n^\ell(R), \quad \rho^\mu(R, \phi) = e^{i\ell\phi} \mathcal{D}_n^\ell(R), \quad (20)$$

in which the label  $\mu = (n, \ell)$ . We assume that the radial functions,  $\mathcal{U}_n^\ell$  and  $\mathcal{D}_n^\ell$ , are real. If they are chosen well then we will be able to capture the relevant physics of the perturbation of interest using only a small number of coefficients, which will minimise the number of elements we need to include in the kernel  $\mathcal{K}^{\mu\nu}$  (equation 11). In this paper we consider two different choices for these basis functions.

#### 3.1.1 Kalnajs Basis Functions

The first is the well-known [Kalnajs \(1976\)](#) basis, which is constructed to satisfy the biorthogonality relation

$$-\frac{1}{2\pi} \int_0^{R_{\text{max}}} \mathcal{D}_{n_1}^\ell(R) \mathcal{U}_{n_2}^\ell(R) R dR = \delta_{n_1, n_2}. \quad (21)$$

Then the matrix  $\mathcal{E}^{\mu\nu}$  that appears on the right-hand side of (8) is simply  $\mathcal{E}^{\mu\nu} = \delta^{\mu\nu}$ . By construction, the density functions  $\mathcal{D}_{n, \ell}(R)$  are equal to zero for radii  $R > R_{\text{max}}$ . We take  $R_{\text{max}} = 15R_0$ . Appendix B reviews this basis in more detail.

#### 3.1.2 Gaussian Basis Functions

Our second way of representing the density and potential is inspired by [De Rijcke et al. \(2019\)](#). For the density basis functions we take

$$\mathcal{D}_n^\ell(R) = \frac{1}{G \sqrt{2\pi\sigma_n^2}} \exp \left[ -\frac{(R - R_n)^2}{2\sigma_n^2} \right], \quad (22)$$

in which  $R_n$  sets the centre of the  $n^{\text{th}}$  basis function and  $\sigma_n$  its width.

The corresponding potential function is the convolution of the density with the Green's function of Poisson's equation. Using §3.11 of [Jackson \(1999\)](#) we may express the latter as

$$\frac{-1}{|\mathbf{x}' - \mathbf{x}|} = -\frac{2}{\pi} \sum_{m=-\infty}^{\infty} \int_0^{\infty} \cos[k(z - z')] e^{im(\phi - \phi')} I_m(kR_<) K_m(kR_>) dk, \quad (23)$$

where  $R_< = \min(R, R')$  and  $R_> = \max(R, R')$  and  $I_m$  and  $K_m$  are modified Bessel functions of the first and second kind respectively. We note that this expression satisfies the boundary condition that the potential be finite at the origin and zero at infinity. For a razor thin disc, the density function of a potential-density pair will be non-zero only in the plane  $z = 0$ . Therefore we can write its  $z$  dependence as  $\rho^\nu(R', \phi', z') = \rho^\nu(R', \phi') \delta(z')$ . Integrating out the  $\phi'$  and  $z'$  with [Equation 23](#) gives

$$\mathcal{U}_\ell^n(R) = -4 \int_0^\infty \left[ \int_0^\infty I_\ell(kR_<) K_\ell(kR_>) dk \right] \mathcal{D}_\ell^n(R') R' dR' \quad (24)$$

where we have taken the value of the potential at  $z = 0$  and focused on a single angular harmonic  $e^{i\ell\phi}$ .

Strictly speaking, as these functions do not span the full set of responses to arbitrarily fine resolution – which is chosen a priori by the widths  $\sigma_n$  of the functions (22) – they do not constitute a basis. Nevertheless, we refer to the functions as ‘basis’ elements.

Unlike the Kalnajs basis, these offer the possibility of tailoring the details of the basis to optimise the sampling both of the imposed perturbation and its response. We do not investigate that possibility here, but instead adopt a simpler approach in line with [De Rijcke et al. \(2019\)](#). To ensure good sampling of the potential response at small radii, where the density is largest, we space  $R_n$  logarithmically between  $0.50R_0$  and  $15R_0$ . The width,  $\sigma_n$ , is picked such that  $R_n + \sigma_n = R_{n+1}$ , making each basis function unresolved. Unlike the Kalnajs basis, these basis functions are not bi-orthonormal, but it is straightforward to use (8) to calculate  $\mathcal{E}^{pq}$ .

### 3.1.3 General comments

In practice we cannot use a complete basis for numerical calculations. The truncation of the basis introduces an effective minimum spatial scale below which perturbations cannot be resolved: for the Gaussian basis functions, this minimum resolution is set by  $\sigma_n$ ; for the Kalnajs basis, the resolution is approximately  $R_{Ka}/n_{\max}$ , where  $R_{Ka}$  is the basis scale radius (Appendix B) and  $n_{\max}$  is the maximum value of the radial index  $n$ . The tapered Mestel disk's stability is highly sensitive to the inner taper ([Evans & Read 1998](#)), the basis functions must therefore be able to resolve this fine structure at small radii; if not, spurious instabilities can develop.

One must also ensure that the perturbation can be sufficiently well resolved at larger radii. For the Kalnajs basis functions, for which the resolution increases linearly with  $n_{\max}$ , ensuring good resolution of the inner taper will ensure a good resolution of any external perturbation over the whole disk. However for our choice of Gaussian basis functions, for which resolution increases only logarithmically with more basis functions, one has to pay more attention. By comparing the true perturbation with its representation in the basis functions one can ascertain if the number of basis functions needs to be increased. We discuss this matter further in section 3.2, where we compare the two sets of basis functions.

Given our basis, we must be able to project  $\psi^e(\mathbf{x})$  on to it. To do so we choose the coefficients  $A_\mu$  that minimise the mean-square error  $\int |\psi^e - A_\mu \psi^\mu|^2 d\mathbf{x}$  by solving the system of equations

$$\mathcal{P}^{\mu\nu} A_\nu = \int d\mathbf{x} \psi^\mu \star \psi^e, \quad (25)$$

in which the matrix

$$\mathcal{P}^{\mu\nu} = \int d\mathbf{x} \psi^\mu \star \psi^\nu. \quad (26)$$

One can construct a similar set of relationships to fit a density perturbation, rather than potential. By construction of the potential–density pairs and the linearity of Poisson's equation, the fit to a potential will give the same coefficients as the fit to the density which sources that potential (up to numerical error). The choice of basis functions implicitly fixes any gauge freedom of the potential expansion.

### 3.2 Testing the effects of basis choice

As we have just mentioned, we must restrict the number of basis functions used to represent the disturbing potential and the subsequent response of the galaxy. Therefore our model does not in general see the 'true' perturbing potential, nor can it predict all details of the response: instead, both are projected onto our finite basis. To test for systematic bias introduced by this projection one can compare predictions using different bases.

[Figure 2](#) shows the density response when the same perturbation is represented in two different bases. To ensure a fair comparison, both basis functions are expanded to the same order, namely  $n_{\max} = 48$ . The top row shows two different impulsive potentials  $\psi^e(\mathbf{x})$  that were applied to the disc at  $t = 0$ , so that all  $A_\mu(t) \propto \delta(t)$ , with  $\mu = (n, \ell = 2)$  and  $n \leq n_{\max}$ . The spatially extended perturbation on the left-hand side of the figure is given by an  $n = 0$  Kalnajs basis function, which, owing to the structure of the Kalnajs basis functions, is zero beyond  $R = R_{Ka} = 15$ . The more localised perturbation on the right-hand side is given by a Gaussian basis element. The rows underneath each perturbation plot show the time evolution of the corresponding density response, calculated using either the Kalnajs basis (left-hand column) or the Gaussian basis (right-hand column).

For the extended perturbation (left-hand panels), the Gaussian basis functions fail to reproduce the structure at large radii. This is because the central radius of the outer most Gaussian basis function is at  $R = 15$  and therefore the Gaussian basis functions will fail to reproduce structure beyond this. Due to the low density at larger radius, the effect of this on the subsequent evolution is minimal, as illustrated by the strong agreement between the Kalnajs and Gaussian density response. One can also see the imprint of the Gaussian basis functions, with the artificial rings imprinted on the density response. These qualitative observations are confirmed by comparing the fractional mean square error between the two approaches averaged over time. For the spatially extended perturbation we obtained a fractional error of 7.3%, whereas for the local perturbation we obtained a fractional error of 2.7%. The fact that there is close agreement between two different basis functions, both quantitatively and qualitatively, implies that the basis functions expansion has been curtailed at an appropriate order.

## 4 GREEN'S FUNCTION

From [Equation 11](#) it is a straightforward exercise to calculate the Green's function of the density response,  $\mathcal{G}_\rho$ . By definition this  $\mathcal{G}_\rho(\mathbf{x}, \mathbf{x}', t - t')$  is the (density) response at location  $\mathbf{x}$  and time  $t$  to an density perturbation  $\rho^e(\mathbf{x}, t) = \delta(\mathbf{x} - \mathbf{x}')\delta(t - t')$ . By linearity it follows that

$$\rho^f(\mathbf{x}, t) = \int d\mathbf{x}' dt' \mathcal{G}_\rho(\mathbf{x}, \mathbf{x}'; t - t') \rho^e(\mathbf{x}', t'), \quad (27)$$



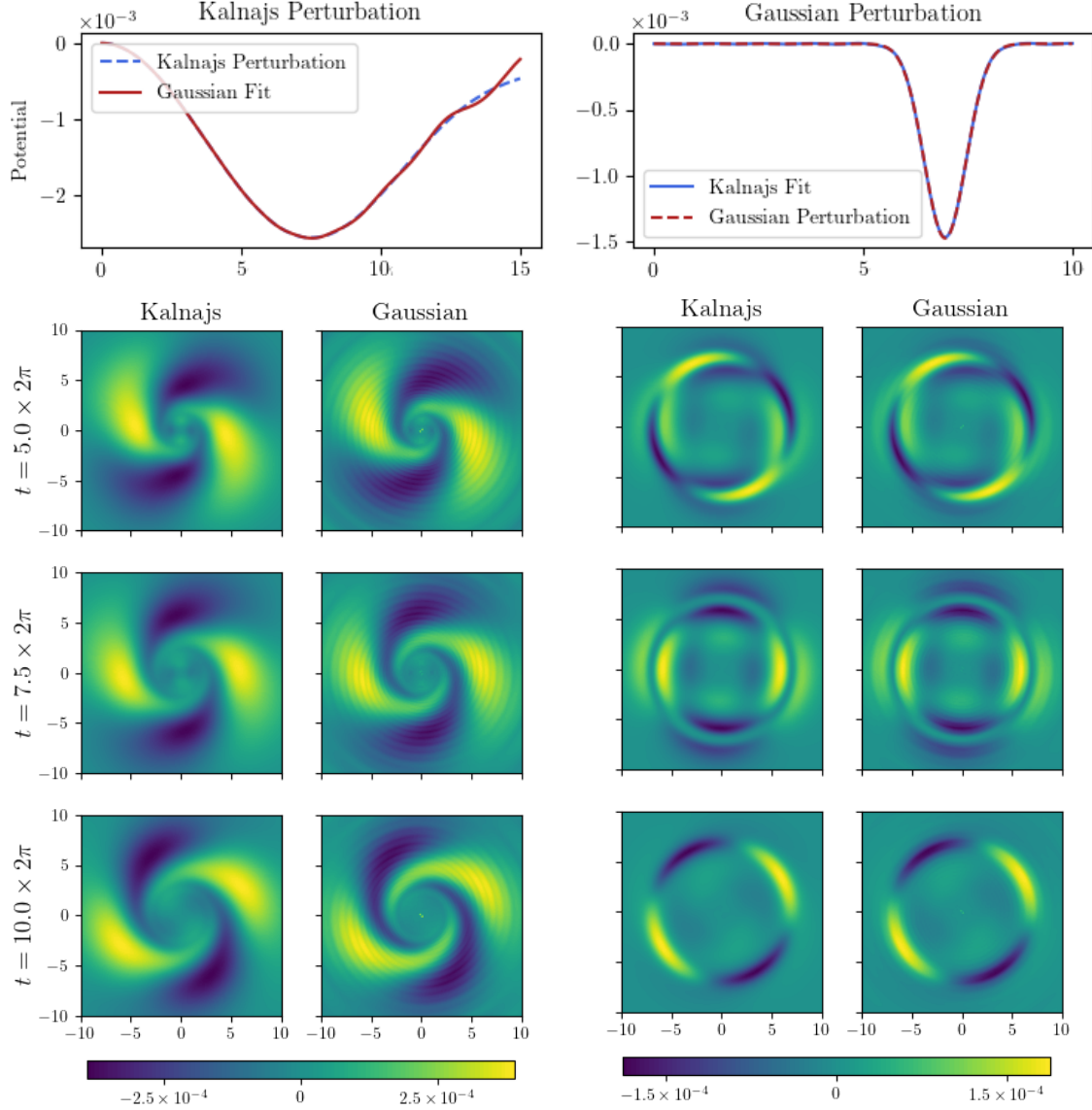


**Figure 2.** Comparing the effect of the choice of basis functions on the computed density response. The top row shows two different  $\ell = 2$  potential perturbations applied at  $t = 0$  together with their representations in the Kalnajs and Gaussian bases. The rows underneath plot the subsequent density evolution computed using the Kalnajs (left) and Gaussian (right) bases. There is strong agreement between the different basis functions. Nevertheless, some imprints from the choice of basis can be seen in the response – in particular the rings from the Gaussian basis functions.

which demonstrates that the Green’s function is the fundamental object for solving initial value problems: one can use it to determine the evolution of the density and potential of the system subject to arbitrary perturbations. From Equation 27 we can obtain  $\mathcal{G}_\rho$  by setting  $\rho^e(\mathbf{x}, t) = \delta(\mathbf{x} - \mathbf{x}')\delta(t - t')$  and then using the formalism developed in section 2 to evaluate the density evolution. To do this we need to express the imposed Dirac delta perturbation as a linear combination of our basis functions. Our basis set is truncated though, which

means that the best we can do is to approximate

$$\delta(\mathbf{x} - \mathbf{x}')\delta(t - t') \approx \delta(t - t') \sum_{\mu} A_{\mu} \rho^{\mu}, \quad (28)$$

as a linear combination of some number  $n_{\max}$  of basis elements. With this approximation we have that

$$\rho_{\mathbf{x}', t'}^f(\mathbf{x}, t) = \int d\mathbf{x}' \mathcal{G}_\rho(\mathbf{x}, \mathbf{x}'; t - t') \sum_{\substack{\mu \\ n \leq n_{\max}}} A_{\mu} \rho^{\mu}(\mathbf{x}') \quad (29)$$

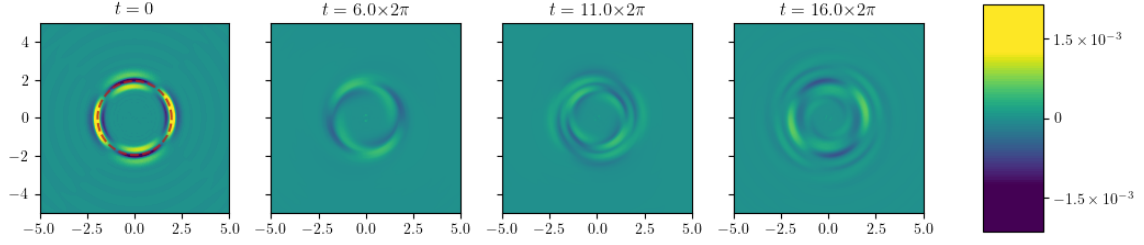


**Figure 3.** The quadrupole harmonic of the Green’s function  $\mathcal{G}_\rho(\mathbf{x}, \mathbf{x}', t)$  for a perturbation at  $\mathbf{x}' = (2, 0)$ , calculated using the Gaussian basis. As this point mass can be decomposed into angular harmonics, this plot shows the quadrupole response of the disk. The red circle indicates the radius over which the perturbation is smeared when the quadrupole harmonic is taken,  $R = 2$ .

and therefore

$$\mathcal{G}_\rho(\mathbf{x}, \mathbf{x}'; t - t') \simeq \rho_{\mathbf{x}', t'}^f(\mathbf{x}, t). \quad (30)$$

We obtain the potential expansion coefficients  $A_\mu$  in (28) by using (25) to fit a Keplerian  $-1/|\mathbf{x} - \mathbf{x}'|$  potential with our Gaussian basis functions. The corresponding density distribution is – to within the resolution limit of our basis – then the Dirac delta that appears in (28). To solve the Volterra equation with an impulsive perturbation we calculate the integral of the perturbative term by hand, reducing the integral equation (11) to

$$\mathcal{E}^{\mu\nu} B_\nu(t) = \mathcal{K}^{\mu\nu}(t) A_\nu(0) + \int_0^t dt' \mathcal{K}^{\mu\nu}(t - t') B_\nu(t'). \quad (31)$$

Figure 3 plots the the quadrupole ( $\ell = 2$ ) harmonic of the resulting Green’s function.

## 5 TORQUE ACTING ON A BAR

In this section we use the formalism developed in section 2 to study dynamical friction within the disk: we perturb the disc by a rotating bar-like potential and calculate the frictional torque that the disc’s response exerts on the imposed bar.

Variants of this problem have been already studied in great detail, making use of both linear response theory and  $N$ -body simulations (e.g. Tremaine & Weinberg 1984; Sellwood 2006; Banik & van den Bosch 2021; Chiba & Schönrich 2022, among others). Lynden-Bell & Kalnajs (1972) first studied the response of a disc to a bar with constant pattern speed, deriving the LBK formula which gives the long-term steady-state linear torque acting on the bar once any transient response has died away. Banik & van den Bosch (2021) applied a similar formalism while relaxing the adiabatic assumption and found that the torque is a combination of two different parts: a transient component and a steady-state component. The transients are damped, not due to a dissipative process, but rather due to the phase mixing of different orbits.

As the transients are inherently a time-dependent phenomena, we can use the formalism laid out in the previous chapter to study more closely the torque they apply to the bar.

When studying a perturbation rotating at a constant pattern speed, linear theory quickly runs in to the problem of trapped orbits. The standard approach to deal with the divergences at resonance is to transform into a frame that rotates at the resonant frequency (pp. 109-117 Lichtenberg & Lieberman 2013), which allows for the construction of a new coordinate system: the so-called ‘slow’ and ‘fast’ actions (e.g. Lynden-Bell & Kalnajs 1972; Tremaine & Weinberg 1984; Chiba et al. 2021). Tremaine & Weinberg (1984) focused on friction in the secular adiabatic limit and showed that only trapped orbits contribute to the total torque on the bar in this regime. As trapped orbits play a key part in the story of bar formation, justifying the linear assumption via comparison to a non-linear prediction is crucial.

In the following section we will outline our bar model. Following that, in subsection 5.2, we will compare linear response theory, and its steady-state torque prediction, to non-linear  $N$ -body simulations in the weak bar regime. In subsection 5.3 we will increase the size of the bar and study the non-linear effects that are introduced in  $N$ -body simulations – most notably orbital trapping.

### 5.1 Bar Models

To calculate the potential profile of our bar we employ the model used in Sormani et al. (2015). In Sormani et al. (2015) a quadrupole potential was generated by a three-dimensional density distribution of the form,

$$\rho_2(r, \phi, \theta) \propto \exp\left(-\frac{2r}{r_q}\right) \sin^2 \theta \cos 2\phi, \quad (32)$$

where  $\{r, \phi, \theta\}$  are spherical polar coordinates with  $\theta = 0$  along the cylindrical  $z$  axis. The parameter  $r_q$  sets the scale length of the bar. As the trigonometric factor in Equation 32 is a linear combination of  $\ell = 2$ ,  $m = \pm 2$  spherical harmonics

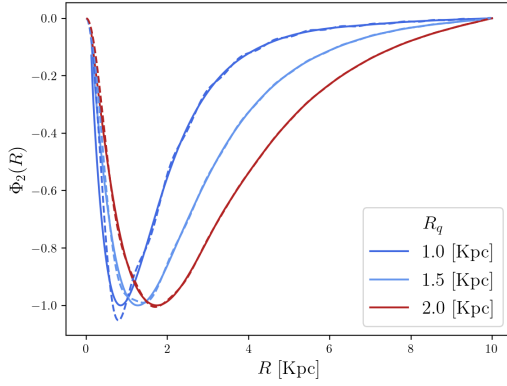


**Figure 4.** The radial potential functions,  $\Phi_2(R)$ , as a function of radius for different scale lengths,  $r_q$ . The solid lines are the radial potential functions calculate solving Poisson's equation with density given in Equation 32. The dotted lines represent the Kalnajs basis function fit using 48 basis functions. We normalise  $\Phi_2(R)$  such that the maximum absolute value of the potential is one so that the strength is all contained in  $\epsilon$ .

$Y_{\ell,m}(\theta, \phi)$ , the corresponding potential is given by

$$\Phi_2(r, \phi, \theta) = \epsilon M(t) \Phi_2(r) \sin^2 \theta \cos 2\phi, \quad (33)$$

where  $\Phi_2(r)$  satisfies

$$\frac{1}{r^2} \frac{d}{dr} \left[ r^2 \frac{d\Phi_2(r)}{dr} \right] - \ell(\ell+1) \Phi_2(r) = \text{const} \times \exp\left(-\frac{2r}{r_q}\right), \quad (34)$$

with  $\ell = 2$ . We use an off-the-shelf boundary value problem solver to find  $\Phi_2(r)$  subject to the boundary conditions  $\Phi_2(r=0) = \lim_{r \rightarrow \infty} \Phi_2(r) = 0$ . We normalise  $\Phi_2(R)$  such that its maximum value is unity, so that the strength of the potential perturbation is solely contained in  $\epsilon M(t)$ .

In order to 'turn the bar on' we let  $M(t)$  be a smoothly increasing function,  $M(t) \in [0, 1]$ . We set  $\theta = \pi/2$  to obtain the potential in the plane, so that

$$\Phi_2(R, \phi) = \epsilon M(t) \Phi_2(R) \cos 2\phi, \quad (35)$$

where we have replaced  $r$  with  $R$  to highlight we are once again in cylindrical polar coordinates. In Figure 4 we plot  $\Phi_2(R)$  for different scale lengths (solid lines) and their reconstruction using the first seventy-two Kalnajs basis functions (dashed lines). The fit works very well, even at small radii.

Our bar model rotates with a constant pattern speed  $\Omega_p$ , so that the perturbation it applies to the disc is simply

$$\Phi_2(R, \phi, t) = \Phi_2(R, \phi - \Omega_p t). \quad (36)$$

In their fit to the observations of our own Galaxy Sormani et al. (2015) report a bar scale length  $r_q = 1.5$  kpc and pattern

speed  $40 \text{ km s}^{-1} \text{ kpc}^{-1}$ . In our model units with  $v_c = 1$  these correspond to  $\epsilon = 0.14$ ,  $r_q = 1.5$  and  $\Omega_p = 0.18$ .

The function  $M(t)$  controls how quickly the bar is turned on. We take

$$M(t) = \begin{cases} 0, & t < 0, \\ \sin^2\left(\frac{t}{4}\right), & 0 \leq t \leq 2\pi, \\ 1, & \text{otherwise,} \end{cases} \quad (37)$$

so that the bar grows over a single dynamical time at the position of the inner taper. We choose this short growth timescale to excite a strong transient response of the disc.

## 5.2 Linear Torque Calculation

For the linear calculation we use the Kalnajs basis functions with 72 terms in the basis expansion, calculating the kernel (12) for 100 time steps with  $\Delta t = 1$ . As we are evolving mean quantities these linear response calculations can adopt much longer timesteps than would be required for an  $N$ -body simulation that has to follow orbits in detail.

The torque acting on the bar is given by

$$\tau_b(t) = \int d^3 \mathbf{x} \rho^e \left[ \mathbf{x} \times (-\nabla \psi^f) \right] = \int d^3 \mathbf{x} \rho^f \left[ \mathbf{x} \times (\nabla \psi^e) \right] \quad (38)$$

where we have used Newton's third law in the final equality to swap the position of the response and the stimulus. As our disc is razor thin, we can represent its 3D response as  $\rho^f(R, \phi, z) = \rho^f(R, \phi) \delta(z)$  (c.f. subsection 3.1), allowing us to trivially evaluate the integral with respect to  $z$ . From the special harmonic structure of the bar (Equation 33), the  $z$  component of the gravitational acceleration due to the bar's potential is zero in the plane of the disc. As the position vector in cylindrical coordinates is  $\mathbf{x} = R \hat{\mathbf{R}} + z \hat{\mathbf{z}}$ , the torque can be simply expressed as

$$\tau_b(t) = \int \rho^f(R, \phi) \frac{\partial \psi(R, \phi)^e}{\partial \phi} R dR d\phi. \quad (39)$$

By expressing the stimulus in potential density pairs, we can analytically evaluate the derivative with respect to  $\phi$ , which results in replacing the derivative with a factor  $i\ell$ . By expanding the response in potential density pairs, and remembering that the density and potential are real quantities resulting from the sum of  $+\ell$  and  $-\ell$  terms, we obtain

$$\tau_b(t) = - \int d\mathbf{x} \left( \mathbf{x} \times \frac{\partial \psi^f}{\partial \mathbf{x}} \right) \rho^e = -2i\ell \mathcal{E}^{\mu\nu} A_\mu(t) B_\nu^*(t), \quad (40)$$

where we have used the orthonormality relation of the potential density pairs to obtain the final equality and we restrict  $\nu = (n_\nu, \ell)$  and  $\mu = (n_\mu, \ell)$ . In this expression we assume that  $\ell > 0$  and introduce the factor of two to account for the  $\ell < 0$  terms in density response and potential stimulus. As  $A_\nu \sim \epsilon$  (c.f. Equation 11) and  $B_\nu \sim \epsilon$  (by definition), this expressions shows that the torque scales as  $\epsilon^2$ . Note that



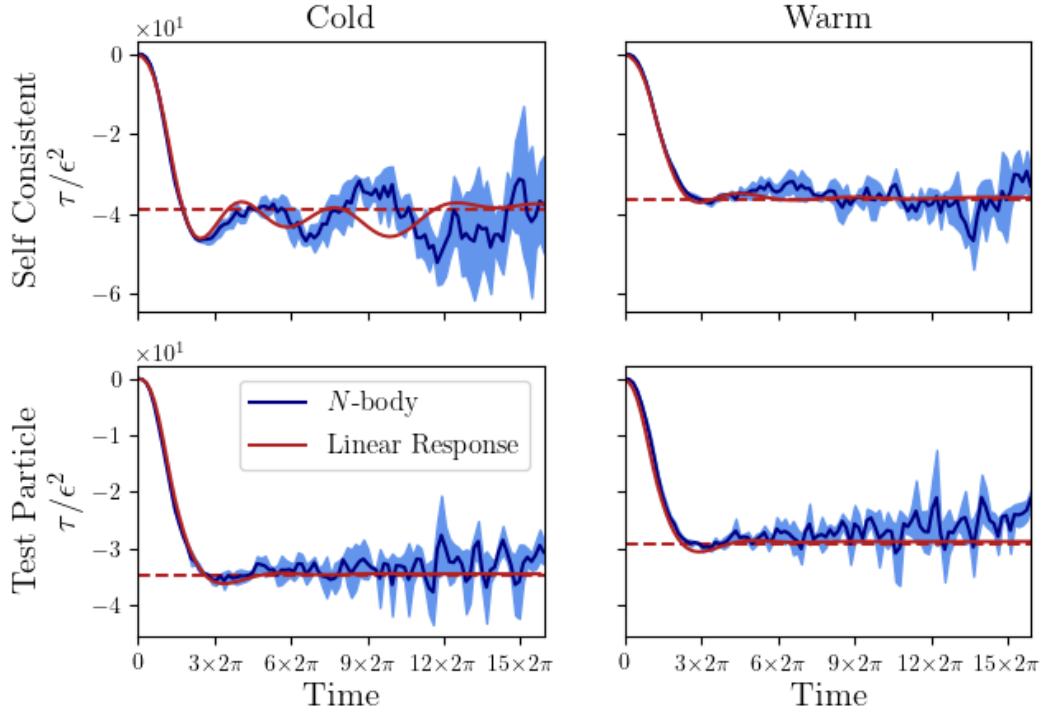


**Figure 5.** The frictional torque (red curve) exerted by discs of different temperatures,  $\sigma_R = 0.35, 0.45$ , when the Sormani bar with  $r_q = 1.5$  is imposed with pattern speed  $\Omega_p = 0.18$ . The top row plots results when the self-gravity of the disc’s response is included, while the bottom row shows corresponding results without self gravity for comparison. The blue curve shows torques measured from three  $N$ -body realisations with  $10^6$  particles, the blue shaded area indicating the standard deviation of these measurements. The horizontal dashed line is the steady-state torque calculated using Equation 44.

as  $A_{n,\ell} = A_{n,-\ell}^*$  and similarly for  $B_{n,\ell}$  it follows that this sum returns a real value for the torque. The form of our bar perturbation (35) means that we need consider only the  $\ell = 2$  contribution.

The resulting torque is plotted in Figure 5 for two different disc temperatures,  $\sigma_R/v_c = 0.35$  and  $0.45$  (left and right columns) and with (top row) and without (bottom row) the self-gravity of the response. We deliberately take  $\epsilon$  to be much smaller than the value for the real galaxy, to ensure that the response is in the linear regime, i.e. so that the terms of  $\sim \epsilon^2$  in Equation 1 remain negligible compared to the linear terms. We will take  $\epsilon = 5 \times 10^{-3}$  for the calculations in this section. We will discuss the issues with setting  $\epsilon$  at a realistic value in subsection 5.3.

The response plotted in Figure 5 shows that the torque from the time-dependent linear response is a combination of two parts: a transient response that quickly damps and a longer-term, constant contribution from the steady-state density wake that trails behind the bar. These two contributions have already been found for bars in halos (Banik & van den Bosch 2021) and for the drag acting on a satellite pulled through the periodic cube (Magorrian 2021). As ex-

pected self-gravity is more important for cooler discs: with less random motion, stars find it easier to ‘unionise’ and work together creating a coherent response, and hence a large torque.

### 5.2.1 An expression for the steady-state torque

We can apply the method used in Magorrian (2021) to calculate the longer term, steady-state torque. After the bar has developed the stirring potential is simply

$$A_\mu(t) = \hat{A}_\mu e^{-i\ell\Omega_p t}, \quad (41)$$

in which the coefficients  $\hat{A}_\mu$  are constant. We assume that the disc is stable, so that, after the transients have died away and the dynamical equilibrium established, its response will be

$$B_\mu(t) = \hat{B}_\mu e^{-i\ell\Omega_p t}, \quad (42)$$

where the coefficients  $\hat{B}_\mu$  are independent of time and dependent linearly on the imposed  $\hat{A}_\mu$ <sup>2</sup>. Making the change of

<sup>2</sup> Notice that an imposed potential of the form (41) would be continually imparting angular momentum to the disc, thereby spinning

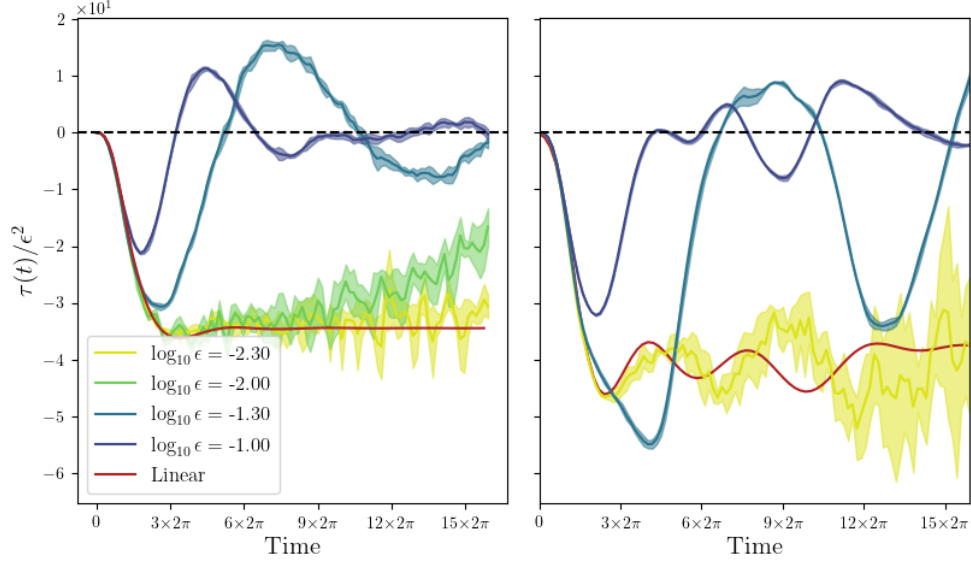


**Figure 6.** The torque acting on the bar due to the response to different strength bars. The left panels shows the test particle response whereas the right panel shows the self-consistent response. The red line shows the linear response calculation. The other lines show the mean  $N$ -body response for different strength bars with three realisations and the shaded area giving one standard deviation. As linear theory predicts a that the torque  $\sim \epsilon^2$ , we normalise by this so that any linear response is independent of  $\epsilon$ . The weak bar agrees well with linear theory, however the response for the larger, more realistic bars quickly become non-linear.

variable  $\tau = t - t'$  in Equation 11 gives

$$\mathcal{E}^{\mu\nu} \hat{B}_\nu = \mathcal{M}^{\mu\nu}(\Omega_p) [\hat{A}_\mu + \hat{B}_\nu]. \quad (43)$$

where  $\mathcal{M}^{\mu\nu}(\Omega_p)$  is the response matrix (Equation 14). It is unsurprising that the response matrix should appear, as by making the assumptions in Equation 41 and 42 we have moved from the time to the frequency domain.

We can now combine our expression for the response in Equation 43 with our general expression for the torque on the bar in Equation 40 to obtain,

$$\tau_b(t \rightarrow \infty) = -i\ell \mathcal{E}^{\mu\nu} \hat{A}_\mu \left[ (\mathcal{E} - \mathcal{M})_{\nu\lambda}^{-1} \mathcal{M}^{\lambda\rho} \hat{A}_\rho \right]^*. \quad (44)$$

an expression that has already been obtained by Weinberg (1989, equation 53) taking a slightly different route.

As the method outlined in section 2 gives the evolution of potential-density coefficients (rather than the perturbation of the DF), we naturally express the torque in these coefficients, leading to a concise expression for the torque. Unlike Banik & van den Bosch (2021), however, but like Weinberg (1989), the expression (44) accounts for the self-gravity of the disc's response via the resonant denominator  $(\mathcal{E} - \mathcal{M})$ .

it up. We follow the usual justification in frequency-based analyses by adding a vanishingly small imaginary component to  $\Omega_p$  so that  $A_\mu(t)$  vanishes as  $t \rightarrow -\infty$ . We can then ignore the angular momentum imparted to the disc, because it scales as  $|A_\mu|^2$ : it is a second-order effect.

We calculate the response matrix using the method outlined in appendix B of (Fouvry et al. 2015), using the same basis set that we use for the kernel calculation. The horizontal dashed lines in Figure 5 plot the torque obtained in this way, showing that it agrees very well with the fully time-dependent linear response calculations. We stress, however, that the real strength of our Volterra method is that it returns the full time dependence, including transients.

### 5.2.2 Comparison with $N$ -body simulation

The results we have just presented are based on a number of approximations. For example, we had to introduce a truncated basis expansion to expand the density and potential response and we neglect the second-order  $[f, \psi]$  term in the CBE (c.f. Equation 1). To test these assumptions we use  $N$ -body simulation to provide an independent measurement of the torque on the bar in which we isolate and evolve the  $l = 2$  response of the disc only. This scheme and the basic operation of our  $N$ -body simulations are discussed in section C.

These  $N$ -body measurements are included in Figure 5. In each panel the Figure plots the mean and standard deviation of the torque measured from three realisations of the disc's response with  $N = 10^6$  particles. The close agreement between the two different methods justifies the assumptions that we have made in our linear response calculations.

Note that, despite the weak strength of the bar, one can

already see some deviations between our linear-response calculation and the  $N$ -body measurements. In particular, the slight drift back towards zero of the test particle simulations is indicative of the nonlinear effect of orbits becoming trapped by the bar potential, thereby spinning up the disc. In order to avoid this effect, we have set the strength of the bar to an artificially weak value. We now study the discrepancy between linear and non-linear results when the strength of the bar is increased to a more realistic value.

### 5.3 Comparison between Linear & Non-linear Theory

#### 5.3.1 Varying the Strength of the Bar

In our previous calculations of the torque we have taken  $\epsilon = 5 \times 10^{-3}$ , despite the realistic value being  $\epsilon = 0.14$ . The reason for this is simple: we wanted to ensure that non-linear effects could be neglected and hence test our linear theory. We will now drop this selfish assumption and study the limitations of linear theory when applied to a bar of realistic strength.

In Figure 6 we plot the torque acting on the bar due to the response to bars of different strengths. We take the same cold disc model as the previous section and set the bar's pattern speed set at a realistic value,  $\Omega_p = 0.18$ . We use three realisations of the  $N$ -body simulations, from which we calculate a standard deviation, which is represented by the shaded region on the plot around the mean. The values of  $\epsilon$  are given in the legend. We normalise the torque by a factor of  $1/\epsilon^2$  as linear theory predicts  $\tau_b \sim \epsilon^2$ . Initially, when non-linear effects have not had time to develop, the normalised torques agree with one another, showing that the response is linear. However, as time progresses, starting with the strongest bar, the  $N$ -body torques begin to depart from the linear response calculation as non-linear effects start to develop. As expected, the nonlinear torques will eventually return to zero, whereas the linear torque approaches a non-zero constant value.

One way of estimating the timescale on which this effect *must* become important is by comparing the torque predicted by linear theory to the disc's total angular momentum: how long before the disc's response becomes comparable to the initial background DF? The initial angular momentum of the cold disc used above is  $L_{\text{disc}} = \int d^2x d^2v L F_0 = 40.4$ . For the largest bar ( $\epsilon = 0.1$ ) the torque at the first turning point is  $\tau \sim 0.45$ . Therefore the time taken for the bar to pump up the disc's angular momentum to 25% of its original value is  $0.25 \times L_{\text{disc}} / 0.45 \sim 3 \times 2\pi$ . Our simulations run for longer than this and therefore we expect to see non-linear effects.

#### 5.3.2 Orbital Sections of Trapped Orbits

If this discrepancy between linear response and  $N$ -body torques is caused by the orbits becoming trapped by the bar (an effect not captured in linear calculations), then we ought

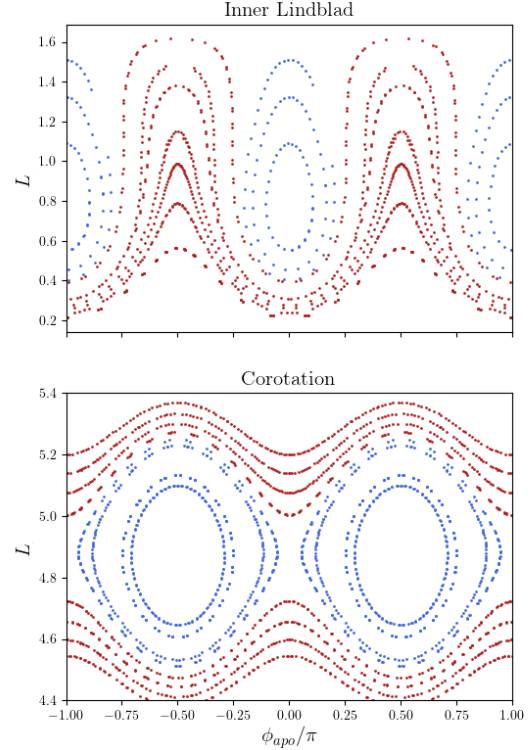


**Figure 7.** Surface of section for a bar with  $\Omega_p = 0.18$ . The upper hand panel shows orbits at ILR and the lower hand panel shows orbits at CR. We plot the angle relative to the bar,  $\phi_{\text{apo}}$ , and the angular momentum,  $L$ , each time the particle passes through apocentre. The trapped orbits, plotted in blue, are radically altered by the perturbation, causing the assumptions of linear theory to breakdown.

to be able to identify these orbits by plotting surfaces of section. To do this we introduce a coordinate frame that rotates with the bar, whose  $Ox'$  axis lies along the bar's major axis. That is, the new  $(x', y')$  coordinates are related to inertial  $(x, y)$  coordinates via

$$\begin{aligned} x' &= x \cos(\Omega_p t) + y \sin(\Omega_p t), \\ y' &= y \cos(\Omega_p t) - x \sin(\Omega_p t). \end{aligned} \quad (45)$$

The corresponding canonical momenta are

$$\begin{aligned} p_{x'} &= \dot{x} - y\Omega_p, \\ p_{y'} &= \dot{y} + x\Omega_p. \end{aligned} \quad (46)$$

The Jacobi integral,

$$H_J = \frac{1}{2}(\dot{x}^2 + \dot{y}^2) + \Phi_0(R) - \Omega_p L, \quad (47)$$

is an integral of motion of stars' orbits in the time-dependent bar-plus-unperturbed disc potential.

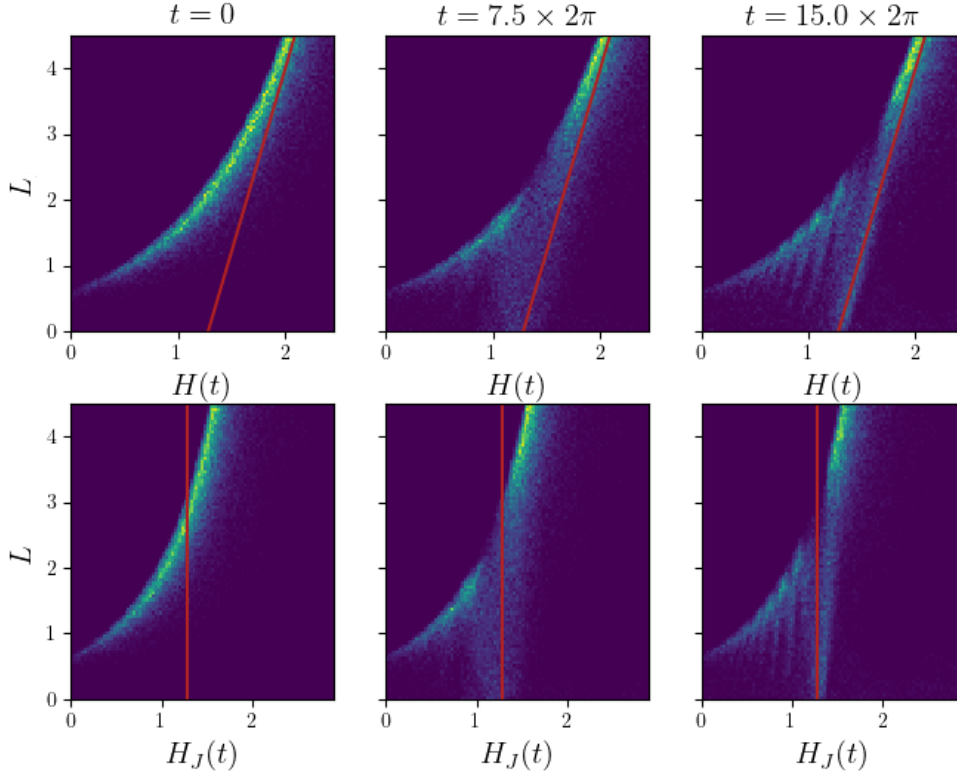


**Figure 8.** The orbits averaged phase space density of the  $N$ -body simulation with  $\epsilon = 0.05$ . The top row shows the phase space as a function of energy,  $E$ , and angular momentum,  $L$ , while the bottom shows the phase space as a function of the Jacobi integral,  $H_J$ , and angular momentum. Particles are driven along lines of constant Jacobi integral by the bar, with particularly large excursions along these lines for trapped orbit. We highlight the line of constant Jacobi integral,  $H_J = 0.69$  associated with the ILR by a red line.

We construct surfaces of section for two regions of phase space, one close to the inner Lindblad resonance (ILR) of the bar, the other at corotation (CR). For each we fix the value of  $H_J$  such that the unperturbed circular orbit's radius is at the location of the resonance. For the ILR the radius  $R_{\text{ILR}}$  of this orbit is found by solving  $2(\Omega(R_{\text{ILR}}) - \Omega_p) = \kappa(R_{\text{ILR}})$ , where  $\Omega(R) = 1/R$  and  $\kappa(R) = \sqrt{2}/R$  are the angular and radial epicycle frequencies of an almost circular orbit of radius  $R$ , respectively. For our bar pattern speed of  $\Omega_p = 0.18$  this gives  $R_{\text{ILR}} = 1.63$  and  $H_{J,\text{ILR}} = 0.69$ . For corotation, the radius  $R_{\text{CR}} = 5.56$  is obtained by solving  $\Omega_p = \Omega(R)$ . The corresponding Jacobi integral  $H_{J,\text{CR}} = 1.21$ .

For each of these regions we sample a variety of initial conditions, from circular to more elliptical, such that they all have the same Jacobi integral. We integrate the orbit from each of these initial conditions in the potential generated by the rotating bar plus the unperturbed disc: that is, we omit the self-consistent response of the disc. At each apocentre passage we record the star's angular momentum  $L$  and its azimuthal angle  $\phi_{\text{apo}}$  measured with respect to the bar's major

axis. The resulting surfaces of section are plotted in Figure 7, with the upper plot showing orbits at ILR, the lower CR. It is immediately apparent that there are two distinct orbit families: circulating, untrapped orbits (red) and librating, trapped orbits (blue). Linear theory is blind to the existence of the latter, which explains why it fails to reproduce the torque of the large bars in Figure 6.

In linear theory we integrate along unperturbed orbits, in essence assuming that, despite any perturbation, the actions remain approximately unchanged. If we wanted to include non-linear effects we would have to update the orbits in light of their reshaping by the perturbation. In Figure 8 we plot the  $(L, E)$  and  $(L, H_J)$  distributions of stars in an  $N$ -body simulation with  $\epsilon = 0.05$  (the livid blue line in Figure 6) at different times. There are dramatic changes in the DF as the system evolves, which cannot be explained using a linear approximation. In particular a stripped pattern develops, which can be seen to occur at fixed Jacobi integral. On the same plot we indicate the lines of constant Jacobi integral,

$H_{J,ILR} = 0.69$  associated with the circular orbit that rotates at ILR in the unperturbed case

## 6 CONCLUSIONS

In this paper we have presented a practical scheme for following the response of 2D stellar discs to internal and external perturbations. Our scheme follows [Julian & Toomre \(1966\)](#); [Seguin & Dupraz \(1994\)](#); [Pichon & Aubert \(2006\)](#) and [Murali \(1999\)](#), among others, by recasting the linearised CBE as a Volterra integral equation of the first kind, which is easy to solve numerically. [Rozier et al. \(2022\)](#) have recently presented a similar application to galactic halos.

There are many studies that solve this integral equation by Fourier transforming in time and considering the response in frequency  $\omega$  instead. There are situations in which this is the natural approach, such as, e.g., testing for stability, or when the galaxy is subject to a periodic perturbation. Nevertheless in most situations the direct approach has a couple of advantages over these frequency-based methods:

- (i) it avoids the difficulties in dealing with the denominator of the response matrix [\(14\)](#);
- (ii) it becomes straightforward to include the effect of the galaxy’s response on an external perturber, making it possible to follow, e.g., the decay of a satellite’s orbit directly (see, e.g., [Magorrian \(2021\)](#) for a simple example).

We have applied the machinery to calculate the dynamical friction torque on an imposed bar. Introducing the bar excites modes that damp quickly, leaving a state in which a steady density wake is established trailing the bar and exerting an constant torque. The colder the disc, the stronger the disc’s density response and the stronger the resulting torque.

We find good agreement with the torques measured from  $N$ -body simulations, as long as the perturbation does not capture many stars on resonantly trapped orbits. The main advantage of the linear response calculation over  $N$ -body simulation is the resolution with which it enables us to study the response: for example, in [Figures 5 and 6](#) the  $N$ -body torques are much noisier than the linear-response ones. Moreover, the linear-response calculation is faster: once the kernels (which depend on the background DF, the basis and the choice of timestep) have been precomputed then solving [equation \(11\)](#) is a matter of seconds, allowing the effect of different perturbations to be studied with ease.

$N$ -body simulation has the advantage, however, of being a much better understood technique and of naturally capturing nonlinear effects (provided, of course, that  $N$  is high enough). The success of the linearized calculation depends on the completeness of the choice of potential–density pairs ([Kalnajs 1976](#)) used to represent the response. We have considered two quite different sets of these, finding that they produce comparable results. An open question is how best to choose them for a given problem (e.g., to minimise the num-

ber of pairs needed to reproduce the self-gravitating response correctly).

No matter how cleverly they are chosen though, they cannot remedy the biggest blindspot of the linearized formalism: the effects of orbit trapping by resonances ([Section 5.3.2](#)). Although there are many applications that are unaffected by this blindspot, an interesting challenge would be to adapt some variant of the machinery presented here that accounts for trapped orbits by perhaps transforming to slow and fast actions (e.g. [Tremaine & Weinberg 1984](#); [Kaasalainen 1994](#); [Sridhar & Tournai 1996](#); [Binney 2016, 2018](#); [Monari et al. 2017](#); [Chiba et al. 2021](#); [Chiba & Schönrich 2022](#)).

## ACKNOWLEDGEMENTS

The authors would like to thank John-Baptiste Fouvry, James Binney, Christophe Pichon and the referee for their insightful comment. This work was supported by the UK Science and Technology Facilities Council under grant number ST/S000488/1.

## DATA AVAILABILITY

The data underlying this article will be shared on reasonable request to the corresponding author.

## REFERENCES

- Al Kazwini H., et al., 2022, *A&A*, 658, A50
- Arnold V. I., 1987, *Mathematical methods of classical mechanics*. Springer, New York
- Banik U., van den Bosch F. C., 2021, *ApJ*, 912, 43
- Binney J., 2016, *MNRAS*, 462, 2792
- Binney J., 2018, *MNRAS*, 474, 2706
- Binney J., Tremaine S., 2008, *Galactic Dynamics*. Princeton university press
- Chiba R., Schönrich R., 2022, *MNRAS*, 513, 768
- Chiba R., Friske J., Schönrich R., 2021, *MNRAS*, 500, 4710
- Colombi S., Sousbie T., Peirani S., Plum G., Suto Y., 2015, *MNRAS*, 450, 3724
- Colpi M., Pallavicini A., 1998, *ApJ*, 502, 150
- De Rijcke S., Fouvry J. B., Pichon C., 2019, *MNRAS*, 484, 3198
- Evans N. W., Read J. C. A., 1998, *MNRAS*, 300, 106
- Fouvry J. B., Pichon C., Magorrian J., Chavanis P. H., 2015, *A&A*, 584, A129
- Jackson J. D., 1999, *Classical electrodynamics*, 3 edn. Wiley
- Julian W. H., Toomre A., 1966, *ApJ*, 146, 810
- Kaasalainen M., 1994, *MNRAS*, 268, 1041
- Kalnajs A. J., 1971, *ApJ*, 166, 275
- Kalnajs A. J., 1976, *ApJ*, 205, 745
- Leeuw F., Combes F., Binney J., 1993, *MNRAS*, 262, 1013
- Lichtenberg A., Lieberman M., 2013, *Regular and chaotic dynamics*. Springer, New York
- Lynden-Bell D., Kalnajs A. J., 1972, *MNRAS*, 157, 1
- Magorrian J., 2021, *MNRAS*, 507, 4840
- Mangeney A., Califano F., Cavazzoni C., Travniecek P., 2002, *Journal of Computational Physics*, 179, 495



Mestel L., 1963, MNRAS, 126, 553  
 Monari G., Famaey B., Siebert A., 2016, MNRAS, 457, 2569  
 Monari G., Famaey B., Fouvy J. B., Binney J., 2017, MNRAS, 471, 4314  
 Murali C., 1999, ApJ, 519, 580  
 Pichon C., Aubert D., 2006, MNRAS, 368, 1657  
 Pichon C., Cannon R. C., 1997, MNRAS, 291, 616  
 Rozier S., Famaey B., Siebert A., Monari G., Pichon C., Ibata R., 2022, ApJ, 933, 113  
 Seguin P., Dupraz C., 1994, A&A, 290, 709  
 Sellwood J. A., 2006, ApJ, 637, 567  
 Sellwood J. A., 2012, ApJ, 751, 44  
 Sellwood J. A., Carlberg R. G., 2014, ApJ, 785, 137  
 Sormani M., Binney J., Magorrian J., 2015, MNRAS, 454, 1818  
 Sridhar S., Tournay J., 1996, MNRAS, 279, 1263  
 Tremaine S., Weinberg M. D., 1984, MNRAS, 209, 729  
 Weinberg M., 1989, MNRAS, 239, 549

## APPENDIX A: CALCULATION OF THE 2D AXISYMMETRIC KERNEL

This section fills in the details of how we calculate  $\psi_{\mathbf{m}}(\mathbf{J})$  and the evolution kernel (Equation 12), closely following the approach taken by Fouvy et al. (2015).

By definition the actions are

$$J_1 = J_r = \frac{1}{\pi} \int_{R_-}^{R_+} dr \sqrt{2(E - \Phi(R)) - L^2/R^2}, \quad (\text{A1})$$

$$J_2 = J_\phi = L, \quad (\text{A2})$$

where  $(E, L)$  are the orbit's specific energy and angular momentum and  $(R_+, R_-)$  are its apo- and peri-centre radii, respectively, which satisfy  $2(E - \Phi(R)) - \frac{L^2}{R^2} = 0$  (e.g. Arnold 1987). Each orbit has a pair of associated frequencies,  $\Omega_1 = \Omega_r$  and  $\Omega_2 = \Omega_\phi$ , which are given by

$$\frac{2\pi}{\Omega_1} = 2 \int_{R_-}^{R_+} \frac{dR}{\sqrt{2(E - \psi(R)) - L^2/R^2}}, \quad (\text{A3})$$

$$\frac{\Omega_2}{\Omega_1} = \frac{L}{\pi} \int_{R_-}^{R_+} \frac{dR}{R^2 \sqrt{2(E - \psi(R)) - L^2/R^2}}. \quad (\text{A4})$$

Given  $\psi(r)$  we can specify an orbit uniquely using any of  $(R_-, R_+)$ ,  $(E, L)$  or  $(J_r, J_\phi)$ . It is straightforward to map from one set of coordinates to the other, except for the map  $(J_r, J_\phi) \rightarrow (E, L)$  which requires the inversion of a non-linear integral map. In practice we transform the integral over  $\mathbf{J}$  in equation (12) to one over  $(R_-, R_+)$ , due to the trivial mapping to other coordinates and because the physical extent of the disk is more naturally expressed in  $(R_-, R_+)$  than in  $(E, L)$ . Directly from the definition of apocentre and pericentre, we have that

$$E = \frac{R_+^2 \Phi_+ - R_-^2 \Phi_-}{R_+^2 - R_-^2}, \quad L = \sqrt{\frac{2(\Phi_+ - \Phi_-)}{R_-^{-2} - R_+^{-2}}}, \quad (\text{A5})$$

where  $\Phi_\pm \equiv \Phi(R_\pm)$ .

The angles associated with the actions (A1) and (A2) are (Lynden-Bell & Kalnajs 1972)

$$\theta_1(R, \phi) = \Omega_1 \int_{C_1[R]} \frac{dR'}{\sqrt{2(E - \Phi_0(R')) - L^2/R'^2}}, \quad (\text{A6a})$$

$$\theta_2(R, \phi) = \phi + \int_{C_1[R]} \frac{(\Omega_2 - L/R'^2) dR'}{\sqrt{2(E - \Phi_0(R')) - L^2/R'^2}}, \quad (\text{A6b})$$

in which  $R$  labels position along the orbit (from pericentre  $R_-$  through apocentre  $R_+$  and back to pericentre) and  $C_1[R]$  is the corresponding integration contour. Tremaine & Weinberg (1984) showed that the basis functions (20) can be expressed as

$$\hat{\psi}_{\mathbf{m}}^{(n, \ell)}(\mathbf{J}) = \delta_{m_2}^\ell \mathcal{W}_{\ell m_2 n}^{m_1}(\mathbf{J}), \quad (\text{A7})$$

thanks to the symmetry assumed in our decomposition of the basis functions (Equation 20). It is important to note that the Kronecker delta means that different angular harmonics decouple, a direct consequence of this decomposition. If the radial function is real then  $\mathcal{W}$  becomes

$$\mathcal{W}_{\ell m_2 n}^{m_1}(\mathbf{J}) = \frac{1}{\pi} \int_{R_-}^{R_+} dR \frac{d\theta_1}{dR} \mathcal{U}_n^\ell \cos[m_1 \theta_1 + m_2 (\theta_2 - \phi)], \quad (\text{A8})$$

in which the transformation of the  $\theta_1$  integral into one over  $R$  introduces a Jacobian

$$\frac{d\theta_1}{dR} = \frac{\Omega_1}{\sqrt{2(E - \Phi(R)) - L^2/R^2}}. \quad (\text{A9})$$

The cosine in (A8) is an even function, which means that  $\mathcal{W}_{\ell m_2 n}^{m_1} = \mathcal{W}_{\ell - m_2 n}^{-m_1}$ , reducing the number of calculations needed. We do the calculation of  $\psi_{\mathbf{m}}^{n\ell}$  for a grid of points in  $(R_-, R_+)$  spaced uniformly with spacing  $\Delta R_{\text{grid}}$ .

Once we have the basis functions we must calculate the kernel (12). As our basis functions are on a grid of points in  $(R_-, R_+)$  space we need to transform the integral measure and derivatives in (12) to reflect the change of coordinates. By the chain rule the derivative with respect to the background DF that appears in (12) is

$$\mathbf{m} \cdot \frac{\partial F}{\partial \mathbf{J}} = m_1 \Omega_1 \left( \frac{\partial F}{\partial E} \right)_L + m_2 \left[ \Omega_2 \left( \frac{\partial F}{\partial E} \right)_L + \left( \frac{\partial F}{\partial L} \right)_E \right]. \quad (\text{A10})$$

We split the Jacobian associated with the change in integration variables from  $(J_1, J_2) \rightarrow (R_-, R_+)$  into two factors. The first is the Jacobian from  $(J_1, J_2) \rightarrow (E, L)$ , which is given by

$$\frac{\partial(J_1, J_2)}{\partial(E, L)} = \frac{1}{\Omega_1}. \quad (\text{A11})$$

The second is the Jacobian from  $(E, L) \rightarrow (R_-, R_+)$ , which is best calculated numerically from (A5). The overall Jacobian is then the product of the two.

Due to the time translation symmetry of the kernel we only

calculate it at a set of points  $t \in [0, \Delta t, 2\Delta t, \dots, t_{\text{end}}]$  where we use a uniform time step,  $\Delta t$ . We typically take  $t_{\text{max}}$  to be of order a few dynamical times. The symmetries of the basis functions (A7) mean that the kernel satisfies the properties

$$\mathcal{K}_{n_p \ell_q}^{n_q \ell_q}(t - t') = \left[ \mathcal{K}_{n_p \ell_q}^{n_q \ell_q}(t - t') \right]^*, \quad (\text{A12})$$

$$\mathcal{K}_{n_p \ell_p}^{n_q \ell_q} = \mathcal{K}_{n_q \ell_q}^{n_p \ell_p}. \quad (\text{A13})$$

We can use these properties to reduce the time required to produce each kernel by approximately a factor of four.

Once we have the kernel we can then use standard techniques to solve the integral equation (11). We use the trapezium rule to approximate the integral on the right-hand side by a sum. Rearranging this sum gives an explicit expression for the response coefficients  $B_\mu$  in terms of their earlier values:

$$B_\lambda(t_n) = \Delta t \left[ \mathcal{E} - \frac{1}{2} \mathcal{K}(t_n) \right]_{\lambda\nu}^{-1} \times \left[ \frac{1}{2} \mathcal{K}^{\nu\mu}(t_n) (A_\mu(0) + B_\mu(0)) + \sum_{i=1}^{n-1} \mathcal{K}^{\nu\mu}(t_n - t_i) [A_\mu(t_i) + B_\mu(t_i)] \right]. \quad (\text{A14})$$

Here we have assumed that the external perturbation  $A_\mu(t)$  is turned on only for times  $t \geq 0$ . The terms involving  $A_\nu(t_i)$  in the right-hand side describe how the external perturbation drives a response in the disk. The  $B_\nu(t_i)$  in the inner square bracket represents the self gravity of the response. We omit these from the sum when comparing to test particle integration.

## APPENDIX B: KALNAJS BASIS FUNCTIONS

In the following section we use the notation of Fouvry et al. (2015). The radial basis functions, introduced in section 2, have two indices: a radial index,  $n_p \geq 0$  and an angular index,  $\ell_p \in \mathbb{Z}$ . The ‘Kalnajs basis’ first described in Kalnajs (1976) have two more parameters:  $k_{\text{Ka}} \in \mathbb{N}$ , which sets the highest polynomial power and a scale radius  $R_{\text{Ka}} \in \mathbb{R}^+$ . For this work we keep  $k_{\text{Ka}} = 4$  and  $R_{\text{Ka}} = 15$ .

The expressions below for the radial part of the basis functions assumes that  $\ell \geq 0$ . Therefore wherever  $\ell$  is here it is presumed to be  $|\ell|$ . In the following we express  $R$  as a dimensionless quantity  $R = R/R_{\text{Ka}}$ . A limited number of the basis functions are plotted in Figure B1. The potential,  $\mathcal{U}_n^\ell(R)$ , and density,  $\mathcal{D}_n^\ell(R)$ , radial functions are

$$\mathcal{U}_n^\ell(R) = -\sqrt{\frac{G}{R_{\text{Ka}}}} \mathcal{P}(k_{\text{Ka}}, \ell, n) R^\ell \times \sum_{i=0}^{k_{\text{Ka}}} \sum_{j=0}^n \alpha_{\text{Ka}}(k_{\text{Ka}}, \ell, n, i, j) R^{2i+2j}. \quad (\text{B1a})$$

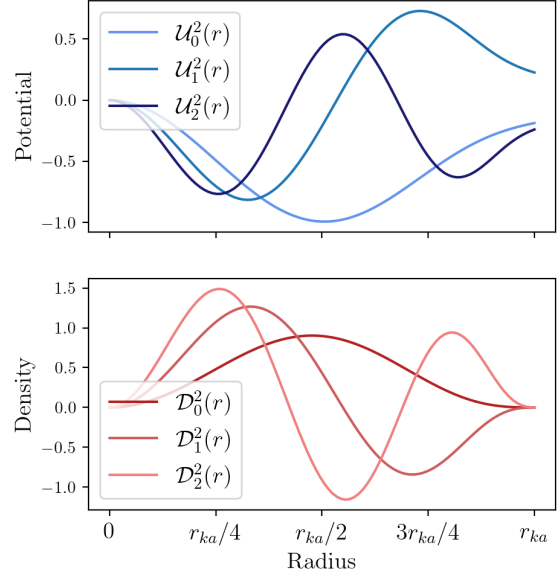


**Figure B1.** The radial part of the Kalnajs basis functions. The top row shows the potential functions,  $\mathcal{U}_n^\ell(R)$ , and the bottom row the density functions,  $\mathcal{D}_n^\ell(R)$ . Each row plots the first three  $n$  modes for a  $\ell = 2$ . The radial scale length is given by  $R_{\text{Ka}}$  which we take  $R_{\text{Ka}} = 20$  for this work.

$$\mathcal{D}_n^\ell(R) = \frac{(-1)^n}{\sqrt{G R_{\text{Ka}}^3}} \mathcal{S}(k_{\text{Ka}}, \ell, n) (1 - R^2)^{k_{\text{Ka}} - 1/2} R^\ell \times \sum_{j=0}^n \beta_{\text{Ka}}(k_{\text{Ka}}, \ell, n, j) (1 - R^2)^j, \quad (\text{B1b})$$

Using the Pochhammer symbol,

$$[a]_i = \begin{cases} 1, & \text{if } i = 0, \\ a(a+1)\dots(a+n-1), & \text{if } i > 0, \end{cases} \quad (\text{B2})$$

the normalisation factors for the potential are

$$\mathcal{P}(k, \ell, n) = \left\{ \frac{\Gamma(2k + \ell + 2n + 1/2)}{\Gamma(\ell + n + 1/2) \Gamma^2(\ell + 1) \Gamma(n + 1)} \right\}^{1/2} \times \Gamma^{1/2}(2k + \ell + n + 1/2) \Gamma(\ell + n + 1/2)^{1/2}, \quad (\text{B3a})$$

$$\alpha_{\text{Ka}}(k, \ell, n, i, j) = \left\{ \frac{[-k]_i [\ell + 1/2]_i [2k + \ell + n + 1/2]_j}{[\ell + 1]_i [1]_i [\ell + i + 1]_j [\ell + 1/2]_j [1]_j} \right\} \times [i + \ell + 1/2]_j [-n]_j. \quad (\text{B3b})$$

The normalisation factors for the density are

$$S(k, \ell, n) = \frac{\Gamma(k+1)}{\pi \Gamma(2k+1) \Gamma(k+1/2) \Gamma^{1/2}(2k+\ell+n+1/2)} \times \left[ \frac{\Gamma(2k+\ell+2n+1/2) \Gamma(2k+n+1)}{\Gamma(\ell+n+1/2) \Gamma(n+1)} \right]^{1/2}, \quad (\text{B4a})$$

$$\beta_{\text{Ka}}(k, \ell, n, j) = \frac{[2k+\ell+n+1/2]_j [k+1]_j [-n]_j}{[2k+1]_j [k+1/2]_j [1]_j}. \quad (\text{B4b})$$

It is worth noting that the calculation of these normalisation coefficients is very costly.

In general when calculating kernels with the Kalnajs basis functions we take the following parameters. The number of terms in our basis expansion  $n_{\text{max}} = 10$ . When calculating the action-angle representation of the potential-density pairs,  $\mathcal{W}_{\ell m_2 n}^{m_1}(\mathbf{J})$ , we do so on a uniform grid in  $(R_+, R_-)$  coordinates, with step size  $\Delta R = 0.15 R_0$  and  $R_+, R_- \leq R_{\text{Ka}}$ . To obtain the kernel from these we sum over  $m_1$ . Therefore we calculate the action-angle representation for of the basis functions for  $-7 \leq m_1 \leq 7$ . We check for stability in all of these parameters and find them to best balance computational speed and accuracy. However, in [subsection 3.2](#), when calculating kernels to compare with Gaussian basis functions we increase the number of basis functions so that  $n_{\text{max}} = 48$ . Due to the finer structure of higher order modes we require a finer grid of  $\mathcal{W}$ , so we take a grid spacing  $\Delta R = 0.08 R_0$ . All the other parameters remain the same.

## APPENDIX C: DETAILS OF TEST-PARTICLE AND N-BODY INTEGRATORS

The following outlines the set up for the  $N$ -body models used in [section 5](#).

We generate initial conditions by first calculating the cumulative radial distribution function,

$$D(< R) = \int_0^R (2\pi R) dR \int d\mathbf{v} F(R, v_R, v_\phi), \quad (\text{C1})$$

where the distribution function,  $F$ , is given in [Equation 19](#). As this includes the tapers, we use the inverse transform sampling method to sample particles' radii  $R_1, \dots, R_N$ . Because our initial conditions are axisymmetric we can choose their azimuthal angles uniformly from  $[0, 2\pi)$ . That sets particles's positions.

The radial components of their velocity are easy to sample:  $v_R \sim \mathcal{N}(0, \sigma_R^2)$ . For each particle, knowing  $R, \phi, v_R$  reduces the DF to a one-dimensional function  $F(v_\phi | R_i, \phi_i, v_{R,i})$ , from which we draw  $v_\phi$  by rejection sampling. We assume that this one-dimensional DF is bounded with  $v_\phi \in [0, v_{\phi, \text{max}}]$  and  $F(v_\phi) \in [0, \mathcal{M}]$ . The upper cut off on  $v_\phi$  is chosen as  $v_{\phi, \text{max}} = v_c + 10\sigma_R$ . We then repeatedly choose trial values of  $v_{\phi,i}$  and  $y_i$ , distributed according to  $v_\phi \sim \mathcal{U}(0, v_{\phi, \text{max}})$  and  $y \sim \mathcal{U}(0, \mathcal{M})$ , until

$y \leq F(v_\phi | R, \phi, v_R)$  at which point we accept the drawn value of  $v_\phi$ .

To each particle we assign a mass  $\mu = M_{\text{disk}}/N$ , where  $M_{\text{disk}}$  is the mass of the active part of the disk and  $N$  is the number of particles.

These initial conditions are evolved using a straightforward particle mesh code. This uses a leapfrog integrator with a fixed global timestep  $\Delta t = 0.01$ . There are three contributions to the potential within which the particles move:

(i) An axisymmetric contribution  $\Phi_0(R)$  that is sourced by the background Mestel disk. This is calculated analytically using  $\Phi_0(R) = v_c^2 \log(R/R_0)$ .

(ii) The potential sourced by the fluctuations in the disk,  $\psi^f(R, \phi)$ .

(iii) The external perturbation that 'stirs' the disk,  $\psi^e(R, \phi)$ .

To include  $\psi^f$  and  $\psi^e$  we use cloud-in-cell interpolation to distribute the particles' mass over a  $120 \times 120$  square mesh that covers  $|x|, |y| < 26$ . We then filter out all but the  $\ell = 2$  Fourier harmonic of this density distribution before using the 'doubling up' Fourier transform method (e.g. [Binney & Tremaine 2008](#)) to convert mesh values from density to potential  $\psi^f$ . To these mesh values we add the contribution of  $\psi^e$ . Then we use finite differencing plus the same cloud-in-cell scheme to obtain the contribution that  $\psi^f + \psi^e$  makes to the acceleration of each particle.

For the test-particle runs (i.e., those that omit the self-gravity of the response) we simply skip the mass assignment step.

This paper has been typeset from a  $\text{\LaTeX}$  file prepared by the author.